J. Fluid Mech. (1996), *vol.* 311, *pp.* 119–140

Instability of oscillatory Stokes–Stewartson layers in a rotating fluid

By JOHN E. HART AND MICHAEL D. MUNDT†

Department of Astrophysical, Planetary and Atmospheric Sciences *and* Program in Atmospheric and Oceanic Sciences, Campus Box 391, University of Colorado, Boulder, CO 80309, USA

(Received 20 June 1995 and in revised form 2 November 1995)

A cylinder rotating about its vertical axis is filled with homogeneous liquid and subjected to oscillatory mechanical forcing. Depending on the ratio, τ, of the forcing period to the spin-down time, the flow adjacent to the sidewall resembles either a classic Stokes layer (small τ), or a modulated Stewartson layer (large τ). Laboratory experiments show that the flow becomes unstable to columnar disturbances that are aligned with the axis of rotation. This azimuthally wavy instability can lead to the formation of strong vertical vortices which penetrate into the interior. Quasi-geostrophic depth-invariant linear instability theory is compared with the experiments. The theory is much too stable and grossly overestimates the experimental critical points. An *inertial adjustment* model, which in a crude way takes account of observed small-scale (ageostrophic) instability and turbulence in the near-wall region, is in much better agreement with the laboratory measurements of the onset of the columnar vortices. Thus, the origin of the vertically coherent structures appears to be crucially related to alterations of the laminar Stokes–Stewartson profiles by fine structure in the boundary layer.

1. Introduction

Laboratory models have often been employed to study the fundamental dynamics of wind-forced ocean gyres. Early experiments (e.g. Beardsley 1969) focused on a sliced cylinder, with steady forcing induced by the differential rotation of a contact lid. When the basic rotation is rapid, the Taylor–Proudman theorem applies and the motions are independent of depth. A uniform bottom slope causes vertical vortex stretching in a manner that simulates the oceanic β-effect. Beardsley (1975) and Krishnamurti (1981), among others, have also conducted experiments illustrating some aspects of time-periodic forcing of such laboratory gyres. In a study aimed at providing data relevant to eddy generation in coastal regions with fluctuating alongshore wind stresses, Pratte & Hart (1991) carried out laboratory experiments on periodically forced flow over non-axisymmetric topography on a polar β-plane. They showed that a barotropic (homogeneous fluid) gyre becomes chaotic after spatially and temporally localized small-scale eddies are generated by instability in the sidewall boundary layer. This particular instability is difficult to analyse because there is no closed-form axisymmetric basic state about which to linearize, and this fact led us to look at a related system with a flat bottom that does have a simple azimuthally invariant time-periodic basic solution $v(r, t)$. The stability of this 'Stokes–Stewartson flow' is of fundamental interest, as it is

† Current address: Institute of Marine Sciences, University of California, Santa Cruz, CA 95064, USA.

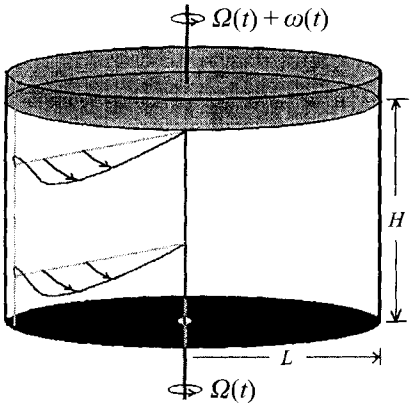

FIGURE 1. Sketch of the experimental apparatus. A right cylinder is rotated about its axis at rate $\Omega(t)$, while the top disc that is immersed in the fluid rotates differentially at rate $\omega(t)$. The fluid is of uniform density and viscosity. All bounding surfaces are rigid.

a generalization to rotating finite-depth fluids of the classic oscillatory Stokes layer stability problem, and provides, as discussed below, an interesting interaction between large-scale flow instability and small-scale turbulence.

We consider motion in an enclosed rotating cylinder subject to weak oscillations in the basic rotation rate Ω about the time-mean Ω_0. Additional driving is provided by differential rotation of a contact lid. This contains a relatively small steady component $\bar{\omega} \ll \Omega_0$, plus, potentially, a modest time-periodic oscillation. The situation is shown in figure 1. A homogeneous liquid with viscosity ν is contained in a tank of height H and radius L. The basic rotation is given by

$$\boldsymbol{\Omega} = \Omega \hat{\boldsymbol{z}} = \Omega_0(1 - \delta_1 \sin(\gamma t))\,\hat{\boldsymbol{z}}, \tag{1}$$

while the differential lid rotation rate is taken to be

$$\omega(t) = \bar{\omega} + \delta_2 \Omega_0 \cos(\gamma t), \tag{2}$$

where γ is the modulation frequency, $\bar{\omega}$ the mean forcing, and the δ are the non-dimensional amplitudes of the basic and differential rotation modulations. We use coordinates attached to the cylinder bottom and sidewall. The Navier–Stokes equations in this frame of reference are (e.g. Hart 1990)

$$\frac{\partial \boldsymbol{v}}{\partial t} + \boldsymbol{v}\cdot\nabla\boldsymbol{v} + 2\Omega(t)\,\hat{\boldsymbol{z}} \times \boldsymbol{v} = -\nabla p + \nu\nabla^2\boldsymbol{v} + \boldsymbol{r} \times \frac{\mathrm{d}\boldsymbol{\Omega}}{\mathrm{d}t}, \tag{3a}$$

$$\nabla \cdot \boldsymbol{v} = 0, \tag{3b}$$

where p is the dynamic pressure divided by the uniform density ρ, z is the vertical (or axial) coordinate, and $\boldsymbol{r}$ is the position vector.

We define a mean flow Rossby number,

$$R_o = \bar{\omega}/2\Omega_0, \tag{4a}$$

a Rossby number for sloshing caused by the oscillation of the basic rotation,

$$R_\Omega = \delta_1/2, \tag{4b}$$

and a Rossby number relating the modulation frequency to the mean rotation,

$$\gamma_m = \gamma/2\Omega_0, \tag{4c}$$

When all these numbers are small the flow is geostrophic and depth-invariant to lowest order. The vertical vorticity equation obtained from (3*a*) may then be integrated from the bottom to the top, where Ekman suction velocities w_b and w_t associated with thin horizontal boundary layers on the horizontal discs are applied. We obtain

$$\frac{\partial \nabla^2 \Psi}{\partial t} + \mathrm{J}(\Psi, \nabla^2 \Psi) = \frac{2\Omega_0}{H}(1 - \delta_1 \sin(\gamma t))(w_t - w_b) + \nu \nabla^4 \Psi + 2\delta_1 \Omega_0 \gamma \cos(\gamma t), \quad (5)$$

where $\Psi(r, \theta, t)$ is the geostrophic streamfunction for the horizontal depth-invariant flow, and J is the Jacobian advection operator.

The standard Ekman compatibility relations just outside the Ekman layers give

$$w_t = \left(\frac{\nu}{4\Omega_0}\right)^{1/2} (2\omega - \nabla^2 \Psi), \quad (6a)$$

and

$$w_b = \left(\frac{\nu}{4\Omega_0}\right)^{1/2} \nabla^2 \Psi. \quad (6b)$$

Introducing scales γ^{-1} for time, γL for velocity, and L for horizontal length leads to the non-dimensional form of the quasi-geostrophic vorticity equation

$$\frac{\partial \nabla^2 \Psi}{\partial t} + \mathrm{J}(\Psi, \nabla^2 \Psi) = -Q(1 - \delta_1 \sin(t))\left(\nabla^2 \Psi - \frac{\bar{\omega}}{\gamma}\right) + E \nabla^4 \Psi + \frac{(\delta_1 + \frac{1}{2} Q \delta_2) \cos(t)}{\gamma_m}. \quad (7)$$

Because δ_1 is small we may neglect the modulation of the stretching term on the right of (7). This leaves four governing parameter groups. These include

$$Q \equiv 2(\nu \Omega_0)^{1/2} / \gamma H, \quad E \equiv \nu / \gamma L^2, \quad \bar{\omega}/\gamma, \quad (8)$$

which are, respectively, the ratio of the spin-down rate to the driving frequency, the lateral Ekman number based on driving frequency (which may be interpreted as a ratio of forcing period to the time it takes a viscous signal to traverse the cylinder), and the non-dimensional mean flow forcing amplitude. The last term in (7) shows the equivalence of periodic lid forcing and modulation of the basic rotation rate of the tank in generating oscillatory flows in the container. Only the second mode of oscillatory driving was used in our laboratory experiments, which have $\delta_2 = 0$. However, in what follows it is useful to define a general forcing function

$$\delta \equiv \delta_1 + \tfrac{1}{2} Q \delta_2, \quad (9)$$

whence the final parameter group becomes δ/γ_m and the approximate quasi-geostrophic vorticity equation may be written

$$\frac{\partial \nabla^2 \Psi}{\partial t} + \mathrm{J}(\Psi, \nabla^2 \Psi) = -Q\left(\nabla^2 \Psi - \frac{\bar{\omega}}{\gamma}\right) + E \nabla^4 \Psi + \frac{\delta}{\gamma_m} \cos(t). \quad (10)$$

In this paper we concentrate on a limited, but typical, range of laboratory parameters in which E is very small, Q is somewhat less than one, and δ/γ_m and $\bar{\omega}/\gamma$ are varied. In the experiments we fix all but $\delta = \delta_1$ and $\bar{\omega}$, and with the other laboratory variables as given in §2 below, all of the parameter groups in (10) can be reconstructed if need be.

The reader may note that the derivation of (10) hinges on depth independence of the dominant parts of the flow. This z-invariance may not hold in a thin '$E^{1/3}$' layer (actually of thickness $E^{1/3} L^{2/3} \gamma_m^{2/3} H^{-2/3}$ using our notation) next to the sidewall. This

latter parameter is of order 10^{-2} in the experiments reported here, so that the contributions from such a region if the flow is in the Stewartson regime ($Q > 1$ for oscillatory motions or $\bar{\omega}/\gamma \neq 0$) takes up only about 10% of the sidewall boundary layer domain. When Q is small, the periodic component of the sidewall flow is dominated by oscillatory Stokes flow, and the '$E^{1/3}$' layer is insignificant.

Equation (10) has an exact solution, because for axisymmetric flow in a cylinder the Jacobian operator vanishes and the resulting forced linear problem is easily solved. The periodic azimuthal flow that will be established some time after turning on the oscillatory driving is described by

$$v(r,t) = \frac{\bar{\omega}}{2\gamma}\left(r - \frac{I_1(r/\eta)}{I_1(\eta^{-1})}\right) + \frac{\delta}{2\gamma_m(1+Q^2)}\left\{r\sin(t) + rQ\cos(t) - \mathrm{Re}\left((Q-\mathrm{i})I_1\left(\frac{r}{\lambda}\right)\frac{\exp(\mathrm{i}t)}{I_1(\lambda^{-1})}\right)\right\}, \quad (11)$$

where the parameters

$$\eta \equiv (E/Q)^{1/2}, \quad \lambda \equiv (E/(Q+\mathrm{i}))^{1/2} \quad (12)$$

are the Stewartson layer and Stokes–Stewartson layer 'thicknesses' respectively. I_1 is a modified Bessel function. A more convenient asymptotic form is obtained when η and $|\lambda|$ are small. This is

$$v(r,t) \approx \frac{\bar{\omega}}{2\gamma}(r - \mathrm{e}^{(r-1)/\eta}) + \frac{\delta}{2\gamma_m(1+Q^2)}\{r\sin(t) + Qr\cos(t) - \mathrm{e}^{a^{1/2}(r-1)}[\sin(t + b^{1/2}(r-1)) + Q\cos(t + b^{1/2}(r-1))]\}, \quad (13)$$

where

$$a = \frac{(1+Q^2)^{1/2}+Q}{2E}, \quad b = \frac{(1+Q^2)^{1/2}-Q}{2E}. \quad (14)$$

Thus, there is a steady bias associated with a Stewartson (1957) layer near $r = 1$ (the first term on the right of (13)). The oscillatory forcing excites a periodically sloshing solid rotation in the interior of the fluid, accompanied by a mixed Stokes–Stewartson boundary layer adjacent to the rigid sidewall in order to bring the tangential flow to zero there. As $Q \to 0$, this latter boundary current reduces to the classic Stokes layer (Stokes 1851), if viewed from a coordinate system rotating at the mean rate Ω_0. When Q is large the solution corresponds to a temporally modulated Stewartson $E^{1/4}$ layer.

Previous two-dimensional calculations by von Kerczek & Davis (1974) have indicated that the pure Stokes layer may be linearly stable as $L \to \infty$. One original goal of our research was to conduct laboratory experiments with varying Q to see if any instabilities found near $Q \approx 1$ might disappear as Q is made small. We thought the problem could also be addressed by solving the linear stability problem for the columnar (depth-independent) modes of instability, which is obtained from (10) while using (11) as a basic state. To our surprise this linear stability problem is largely irrelevant to what is seen experimentally, because instability is observed for a much lower forcing amplitude than that for which the linear theory has unstable solutions. Similar comparisons have been made for the non-rotating Stokes problem (von Kerczek & Davis 1974; Davis 1976). They suggest that the laboratory flows become prematurely unstable due to finite-amplitude perturbations and nonlinear instability. In our rotating-fluid case, the observations of low-δ/γ_m columnar eddy generation can be adequately explained by an *adjusted linear stability theory* that takes into account

the effects of small vertical-scale (non-columnar) near-wall turbulence that significantly changes the vertically invariant zonal flow upon which the columnar instabilities grow.

2. Experimental results

The experiments were conducted in a Plexiglas cylinder of radius $L = 22.8$ cm and depth $H = 26.0$ cm, using water with a nominal viscosity of 0.01 $cm^2\ s^{-1}$. The mean rotation period was fixed at 2.5 s ($\Omega_0 = 2.51$ rad s^{-1}). The dimensionless modulation frequency γ_m was 0.025 (period = 50 s), although a few runs were made with other values. For reference these numbers give $E = 1.6 \times 10^{-4}$ and $Q = 0.097$. This puts us in the Stokes–Stewartson boundary layer regime in which, for $\bar{\omega} = 0$, the Stewartson contribution is relatively small. Visualization was by videography of a Kalliroscopic platelet suspension. While this method is somewhat crude for detecting small-amplitude disturbances, given the huge disparity between the experiments and linear theory, and the mildly model-dependent 'inertial adjustment' stability calculation presented in §4, it seems sufficient for illustrating the main points of this paper. Two video cameras were employed, one looking down on the transparent top lid, and one looking in along a radius at mid-height. The whole system was mounted on a rotating turntable. A servo loop maintained stability of the basic rotation to better than 0.01 %, and the differential lid rotation was accomplished by sending an analog voltage to a voltage-controlled oscillator that, in turn, drives a stepper motor attached to the tank. All rotation rates are controlled by a digital computer program in a manner that permits easy implementation of relations like (1) and (2). Changes in parameters were followed by a waiting period of about 20 forcing cycles. After this delay, a segment of videotape was recorded and subsequently scanned for θ-dependent waves and vortices near $r = 1$, when looking down from the top. Steps in δ were usually around 10 %. Unit jumps in the differential basic rotation parameter $\bar{\omega}/\gamma$ were taken in order to qualitatively illustrate the dependence of columnar wavy instability on the size of the mean rotation.

Figure 2(*a*) shows an instability in the wall layer at a slightly supercritical parameter setting. The first observation of waves during a forcing cycle is typically slightly before the time of minimum rotation rate of Ω, which occurs at $t = \frac{1}{2}\pi + 2j\pi$, $j = 0, 1, 2, 3, \ldots$. This usually corresponds to the highest co-rotating (cyclonic) flow just outside the wall boundary layer. The direction of the mean rotation rate Ω_0 defines 'cyclonic'. As the rotation $\Omega(t)$ hits its minimum, the initial waves in the near-wall region amplify quickly and vortices move into the interior (figure 2*b*). The vortices have a characteristic tilt in the prograde direction moving inwards from the wall. By looking up at the bottom glass plate while at the same time viewing from the top, or by looking in from the side (figure 5*a*) it is ascertained that the vortex structures shown in figure 2 are vertically coherent. This z-independence is expected because conditions for applicability of the Taylor–Proudman theorem are reasonably well satisfied for these mesoscale eddies. The timing of the instability is only weakly dependent on $\bar{\omega}$. For example, when $\bar{\omega}/\gamma = -6.0$, and $\delta/\gamma_m = 4.8$, vortices first become obvious at $t = 0.63\pi$, reach maximum amplitude at $t = 0.83\pi$, and then decay away shortly after $t = 1.17\pi$.

The vortex penetration phase at mildly supercritical conditions is associated with somewhat irregular pairings that tend to lower the total wavenumber. Depending on the parameters, vortices can migrate deep into the interior and persist for more than one cycle, leading to large-scale quasi-geostrophic turbulence with eddy scales that are some modest fraction of L. Conditions favouring this are relatively small γ, which corresponds to long-time-scale forcing, and, of course, relatively large δ. If γ is too big,

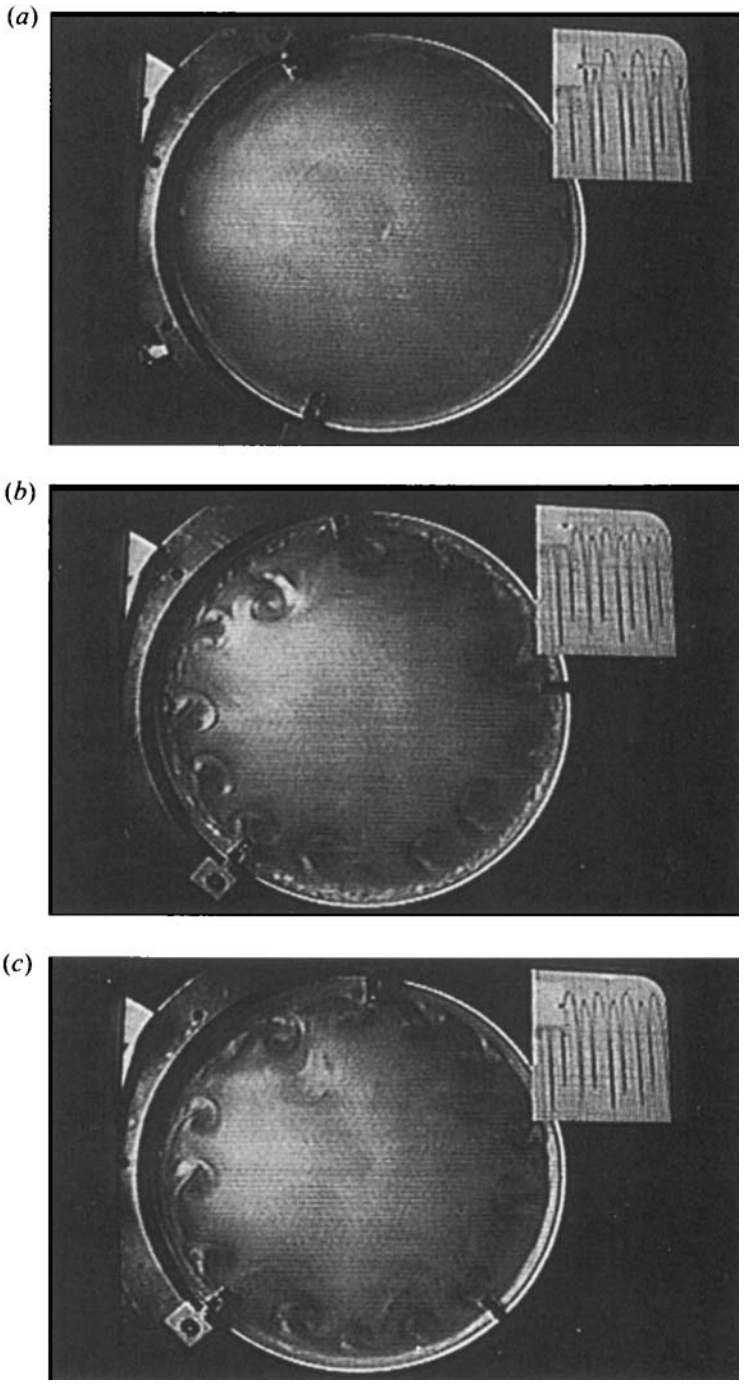

FIGURE 2. Images from the experiment. The basic rotation is clockwise, the view is from the top, and $\bar{\omega}/\gamma = 3.0$. (*a*) $\delta/\gamma_m = 4.5$ at $t = 0.21\pi$. (*b*) $\delta/\gamma_m = 5.8$ at $t = 0.56\pi$. (*c*) $\delta/\gamma_m = 5.8$ at $t = 0.97\pi$.

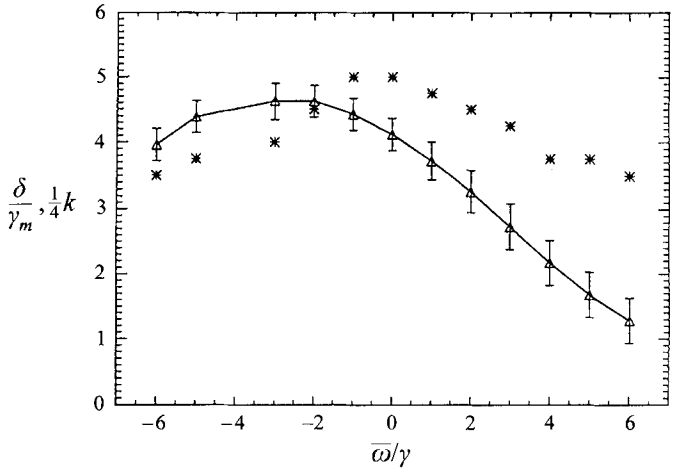

FIGURE 3. A regime diagram for $\gamma_m = 0.025$, $Q = 0.097$, $E = 1.6 \times 10^{-4}$. The solid line gives the transition data for first observation of waves in the boundary layer as δ increases. The stars denote the azimuthal wavenumber (normalized by 4). The wavenumbers are approximate, partly because purely uniform wave trains are rarely observed around the entire circumference, and partly because the wavenumber counts depend on the degree of supercriticality and forcing phase angle.

even if there is instability the flow reverses before there is time for the vortices to enter the interior. If they stay in the boundary layer they dissipate during the maximum rotation phase of the forcing cycle. For example, following the time shown in figure 2(*c*) the interior eddies at this parameter setting fade out and the cycle repeats. On the other hand, for $\gamma_m = 0.006$, with other parameters the same as those in figure 2(*c*), vigorous stirring of the interior by the wall-generated vortices persists over an entire cycle. Hart (1994) provides experimental data and additional qualitative discussion of these points.

Figure 3 summarizes the laboratory data on columnar vortex onset. The solid curve with error bar estimates gives the transition data, with the stable region (no vortices) being below the curve. Several values of mean differential rotation were used. For $\bar{\omega} = 0$ (no mean forcing from the top lid) the instability sets in at $\delta \approx 0.1$ for $\gamma_m = 0.025$ ($\delta/\gamma_m \approx 4$), and has an azimuthal wavenumber of about 20. The azimuthal wavenumber is measured by counting the number of waves circumferentially distributed around the tank when they first become obvious in the video imagery. This wavenumber is usually slightly higher than the number of penetrating vortices. When there is a mean co-rotating component to the differential driving ($\bar{\omega} > 0$), the data in figure 3 show that the critical curve for columnar instability dips to lower values, so that instability occurs at lower modulation δ (at fixed γ). On the other hand, with mean lid rotation opposite to Ω_0 ($\bar{\omega} < 0$) the critical curve is more or less flat, and the instability is only slightly suppressed (relative to $\bar{\omega} = 0$) until $\bar{\omega}/\gamma$ becomes quite negative, where it is enhanced. There are small changes in zonal wavenumber as $\bar{\omega}$ varies, such that a large mean differential co-rotation seems to be associated with slightly longer waves. The most important findings for what follows is the observation that positive differential mean-rotation cases are significantly more unstable than those with zero or negative (counter-rotating) lid motion, and that the columnar instability typically sets in at values of δ/γ_m of about four or less.

Another interesting aspect of the experimental results is that the columnar instabilities occur during only one phase of the forcing cycle, irrespective of $\bar{\omega}$, with

maximum amplification and vortex penetration occurring for time in the range $t = \pi/2$ (minimum Ω) to approximately $t = \frac{3}{2}\pi$ (maximum Ω). This is a little surprising, particularly for $\bar{\omega} \to 0$, because then the profile (11) is antisymmetric. It simply changes direction, not shape, between successive half-periods of the forcing (i.e. $v(r, t+\pi) = -v(r, t)$). A quasi-geostrophic model of the instability (e.g. (10) and (11)) will not have the observed single-phase growth property because instability will be equally likely at two phases of the driving displaced by 180°.

A few additional runs at fixed δ and $\bar{\omega}$, with variable γ, were carried out. The discussion in § 1 indicates that this is a four-parameter problem, and these runs were undertaken to give an idea of what happens to the columnar instability on a non-dimensional γ_m axis normal to the plane of figure 3. For example, in agreement with figure 3, vigorous vortices are generated at $\delta = 0.07$, $\bar{\omega}/\gamma_m = 5$, and $\gamma_m = 0.025$ ($\delta/\gamma_m = 2.8$). However, as γ_m changes, with δ and $\bar{\omega}$ fixed, the vortices disappear for $\gamma_m \lesssim 0.003$ and for $\gamma_m \gtrsim 0.07$. The vortices generated by the instability appear strongest for a value of γ_m of about 0.03. Therefore, the critical stability sheet, through which the curve in figure 3 passes for $\gamma_m = 0.025$, is thought to rise for both substantially smaller and somewhat larger γ_m. Following a discussion of what we believe to be the essential physics of the instability, we offer a possible explanation of this result.

3. Linear instability theory

In an effort to interpret figure 3, perturbation equations were derived, in the cylindrical geometry, from the quasi-geostrophic model (10) by linearizing about the azimuthal basic state (11). The resulting equations are separable in θ so that $\Psi = \phi(r, t)\exp(ik\theta)$ represents the instabilities for various integer zonal wavenumbers k. The complex partial differential equation for $\phi(r, t)$, in which k is a parameter, is solved numerically on a stretched grid using N points in radius and a stretching function that concentrates points exponentially in the sidewall boundary layer near $r = 1$. Suppose the normal radial coordinate is given by

$$r' = \frac{j-1}{N-1},$$

where $j = 1, 2, 3, \ldots, N$. Then the stretched coordinate is given by

$$r = \frac{1-e^{-\alpha r'}}{1-e^{-\alpha}}.$$

Typical values are $N = 200$, $\alpha = 4$. In the figures shown below there are no discernible differences in going up to $N = 520$. Tests with $\alpha = 0$ and 2 indicate that stretching is helpful, but higher values than $\alpha = 4$ are not required. The problem is posed as an initial value calculation in which a random perturbation to ϕ is initiated at $t = 0$. No-slip is enforced at $r = 1$, and a regularity condition is imposed at the origin. The coupled equations for vorticity and streamfunction were time-marched implicitly using a Crank–Nicholson method. The solutions were then obtained via sparse matrix inversion at each time step. The time step is chosen so that sufficient numerical accuracy is obtained. This presents problems at large k ($\gtrsim 50$) and large δ, because then the azimuthal advection of waves is large during parts of the cycle and very small time steps are required. At large time the total kinetic energy of a particular k-mode is monitored over several forcing cycles. If the net energy increases between start and

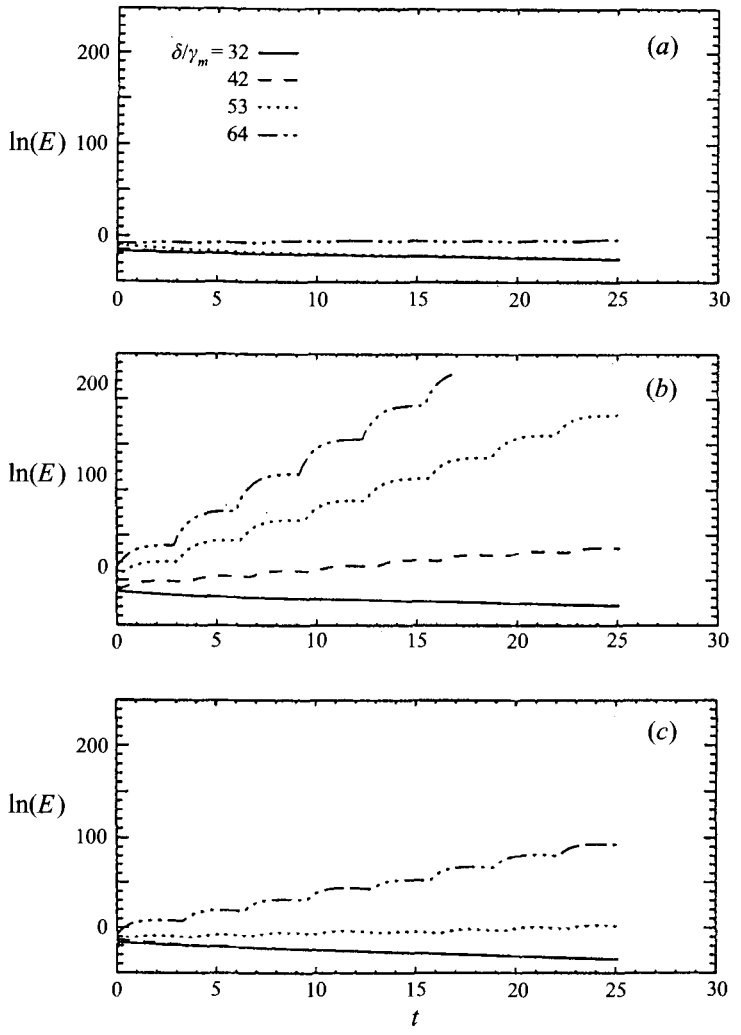

FIGURE 4. Results of the linear instability calculation for the laminar Stokes–Stewartson layer with $E = 1.6 \times 10^{-4}$, $Q = 0.1$, $\gamma_m = 0.025$, $\bar{\omega} = 0$. Natural log of disturbance kinetic energy *vs.* time for (*a*) $k = 10$, (*b*) $k = 20$, and (*c*) $k = 30$ for the values of the forcing shown. The time origin corresponds to about 2 boundary layer diffusion times.

finish of each driving oscillation, then the disturbance is said to undergo 'total instability'. If it rises during any part of the cycle, but finishes lower than it started, the disturbance is said to be 'transiently unstable'.

Figure 4 shows results for $\bar{\omega} = 0$. Instability appears possible for large enough forcing. As anticipated there are two periods of growth for each 2π-long forcing cycle. The transition is quite sudden in the sense that energy amplification factors of order e^{10} over a cycle are possible for supercriticality of order one. The δ/γ_m separation between the total instability traces seen in figure 4 and regions of transient instability is small. It was difficult to find a sizeable range of parameters for which significant transient instability (as defined above) occurs at large times. An initial energy hump or two, due to unbalanced initial conditions, can be seen early in a numerical integration. However, the parameter-space boundary between monotonic energy decay and net energy growth is very sharp at large times. For example, in the $k = 20$ case, the motion

goes from stable at $\delta/\gamma_m = 37$ to transient unstable at $\delta/\gamma_m = 38$, but is already totally unstable at $\delta/\gamma_m = 39$ (with unit steps in parameters). Furthermore, the energy growth per cycle in the transient region is only of order 1. The most important point is that the predicted instability threshold is far larger than the observed values. The theory is about an order of magnitude higher, with a critical value of δ/γ_m of about 39, compared with 4.2 in the laboratory. It is for this substantial discrepancy that we seek a plausible explanation.

Before moving on to our modified theory, two other aspects of this instability problem are of interest. First, von Kerczek & Davis (1974) present linear stability calculations which show that a pure planar Stokes layer ($Q = 0, L \to \infty$) of thickness $\delta_s = (2\nu/\gamma)^{1/2}$ is linearly stable for Reynolds number

$$Re^{\delta_s} \equiv U\delta_s/\nu = \delta/((2E)^{1/2}\gamma_m) < 800, \tag{15}$$

where the 800 figure represents the largest value for which numerical solutions were obtained. They speculate that the Stokes layer may be stable for all Re^{δ_s}. The transition points in figure 4 correspond to a Stokes Reynolds number of about 3500, suggesting that instability may be possible at high enough Reynolds number with finite L. As Q is made smaller in our calculations, the critical δ/γ_m does not change very much. At our laboratory value of $Q = 0.097 \approx 0.1$ the profiles for $\bar{\omega} = 0$ are not strongly influenced by vortex stretching and are close to pure Stokes flow. Upon increasing Q, our calculations show that the motion becomes more stable (i.e. the critical δ increases). This is expected because at large Q the modulated Stewartson layer has no inflection points at all since $b \to 0$ in (13). The second important point about these linear calculations is that because δ is so large for instability this model is almost totally insensitive to mean lid rotations $\bar{\omega}$ in the range studied experimentally.

The traditional quasi-geostrophic approximation is not valid for the large values of δ required for instability in figure 4 if modulation of the entire tank (1) is used to force the motion. One could attempt to fix this up by keeping the $\delta_1 \sin(t)$ term in (7) while still looking at two-dimensional disturbances, but we do not believe this is the source of the problem. Conceptually, the theoretical calculations can be related to an experiment with large periodic lid forcing δ_2 and zero tank-rotation-rate modulation, but then one would have to worry about the validity of the Ekman suction model used to derive (10). In comparing with experiments, we note that linear stability theory using the laminar Stokes–Stewartson basic-state profile fails to predict the observed columnar instability, which in the laboratory occurs in a region of parameter space that has a small value of δ, consistent with the assumptions made in the derivation of the governing equation.

4. Inertial adjustment

The columnar quasi-geostrophic model is invalid in regions where either the requirement of depth-independent motion breaks down, or the assumption that relative vorticity is much smaller than the mean planetary vorticity $2\Omega_0$ fails. The strongest shears are in the vicinity of the sidewall boundary layer. For δ of order 0.1 the local Rossby number for the sidewall layer can be order one. A first possibility is that z-invariant ageostrophic advections due to non-geostrophic interior flow driven by the Ekman suction, as well as additional stretching of total vorticity, cause changes in the structure of the Stokes–Stewartson layer, making it more unstable. This reflects a failure of quasi-geostrophy, while retaining depth-invariance. However, the Ekman-fed ageostrophic flow is of order Q times the local Rossby number, and since this is still

fairly small in most of our experiments it seems unlikely that this mechanism is responsible for the dramatic destabilization (relative to the linear theory of §3) observed in the laboratory flow. It may however modify the instability characteristics, once the instability is established by a different mechanism.

A second possibility is that the motion has two components. There are vortex columns associated with the instabilities as illustrated in figure 2, and there are, in addition, motions with small vertical scale that arise from an ageostrophic depth-dependent instability that is not described by the z-invariant model (10). In this regard we point out that for the system with basic rotation Ω_0 there is no Squires' theorem, and two-dimensional columnar modes will not, of necessity, be the most unstable. This situation may be compared with the non-rotating Stokes layer problem (von Kerczek & Davis 1974) that does satisfy such a theorem, guaranteeing dominance of two-dimensional modes in the unstable eigenvalue spectrum.

Figure 5(*a*) shows a photograph looking through the sidewall. In addition to the columnar disturbances (bright vertical bands) at the left and right sides of the image, there also are streamwise 'longitudinal roll' motions, which appear bent or modulated by the vortex columns. These latter modes are always observed to be present prior to the columnar instability. The longitudinal rolls typically form in the sidewall layer somewhat before the minimum of the basic rotation. Near or just after the minimum in the forcing, the 'inner' part of the sidewall layer adjacent to the wall can become turbulent (figures 5*b* and 5*c*). A close examination of figure 2(*b*) also reveals a narrow band of turbulent fluid near $r = 1$ between the columnar vortices and the boundary.

When η and λ are small, the curvature of the boundary is dynamically insignificant. The roll instabilities observed here are similar to the so-called 'inertial instabilities' that occur in a horizontally sheared flow in a rotating channel (Hart 1971). These arise through an interplay of Coriolis forces associated with a basic rotation Ω_0, and advection of the zonal flow by roll velocities normal to the wall. There is a close analogy between these instabilities and thermal convection rolls, where the dimensional quantity $\Gamma = 2\Omega_0 + \partial\bar{v}/\partial r$ plays the role of the thermal stratification. For example, a necessary condition for roll instability is that Γ, like the vertical thermal gradient in convection, must be negative inside the domain. The condition that $\Gamma < 0$ for roll instability is also related to Rayleigh's absolute angular momentum gradient criterion for the instability of inviscid curved flows. At the experimental parameters for which columnar instability is observed, Γ can be strongly negative. For example, taking the limit of small Q, and using (13) and (14) to described the basic flow, it is straightforward to find the critical value of the forcing needed to satisfy the non-dimensional version of this necessary criterion for instability. With our scaling the $\Gamma < 0$ constraint becomes

$$\frac{\partial \bar{v}}{\partial r} < -\gamma_m{}^{-1} \tag{16}$$

for some value of r in the domain. This condition is first satisfied at $r = 1$ and at $t = \frac{1}{2}\pi$. The critical forcing level needed is then given by

$$\left(\frac{\delta}{\gamma_m}\right)_c = 2E^{1/2}/\gamma_m - \bar{\omega}Q^{1/2}/\gamma. \tag{17}$$

Inserting the values of our fixed experimental parameters yields

$$\left(\frac{\delta}{\gamma_m}\right)_c = 1.02 - 0.31\bar{\omega}/\gamma. \tag{18}$$

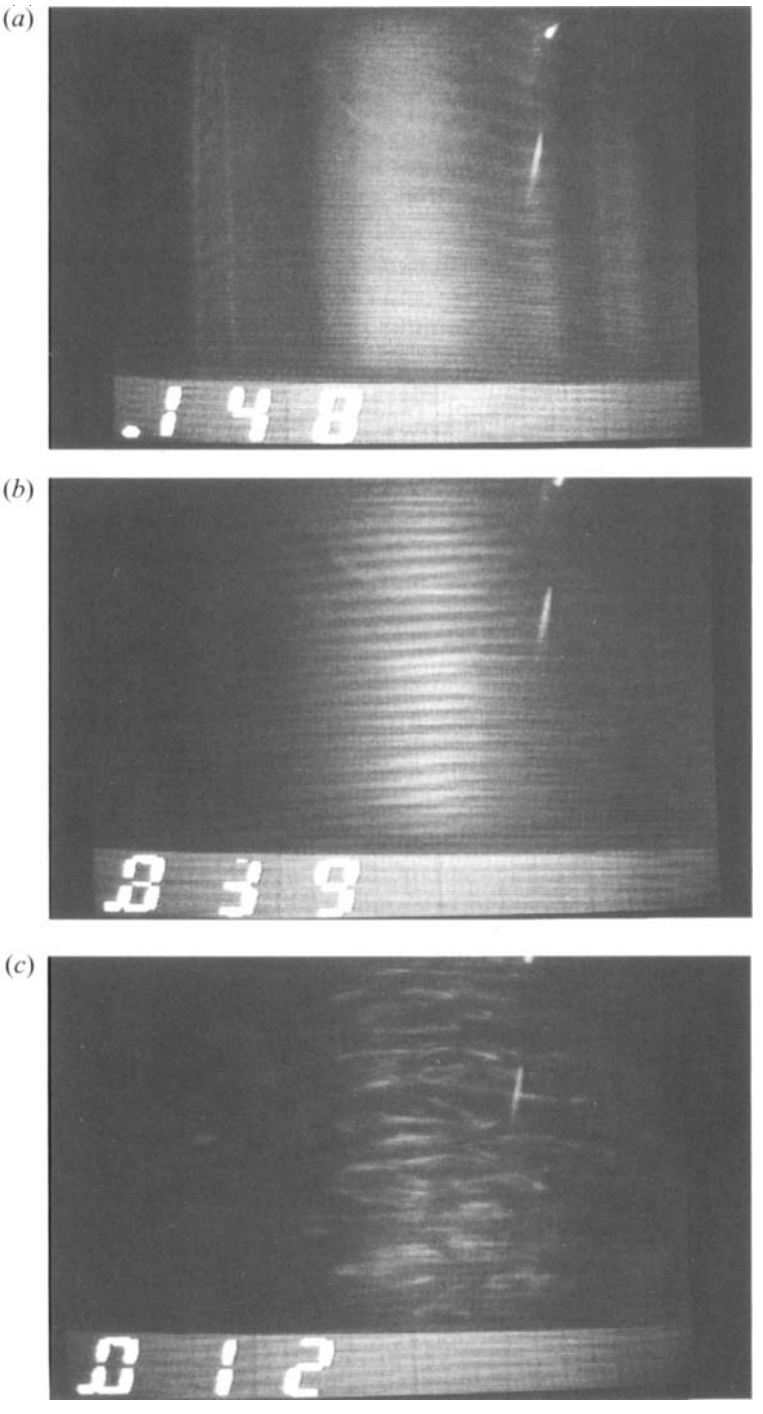

FIGURE 5. (*a*) Photograph looking in through the sidewall showing a region about 15 cm across at mid-depth, with $\bar{\omega}/\gamma = -6.0$, $\delta/\gamma_m = 4.8$ and $t = 0.80\pi$. (*b*) $\delta/\gamma_m = 6$, $\bar{\omega}/\gamma = 1.5$, $t = 0.18\pi$. (*c*) same as (*b*) but $t = 0.52\pi$. The counter measures 2π units of time over the range 0 to 1, with 0 and 1 being times of minima of $\Omega(t)$.

Comparison with figure 3 illustrates that when the columnar instabilities occur, the system is strongly supercritical with respect to the inertial instability condition (except perhaps at large negative values of the mean forcing). The characteristic value of the boundary layer Reynolds number is several hundred, and, as mentioned above, the rolling motions may be turbulent during a substantial fraction of the forcing cycle (figure 5*b*, *c*). If one assumes a connection between the roll-dominated wall-layer turbulence and the columnar instability, (18) provides a rationalization for the observed lowering of the modulation δ needed for vertical vortex generation with positive differential forcing $\bar{\omega}$, relative to that for zero or slightly negative $\bar{\omega}$, as shown in figure 3.

Just as turbulent thermal convection homogenizes the interior temperature in a differentially heated layer, we expect that inertial instability turbulence will nullify Γ. Such an effect has been observed in laboratory experiments and computational simulations of turbulent Poiseuille flow down rotating channels with basic rotation (e.g. Johnston, Halleen & Lezius 1972; Tafti & Vanka 1991). We propose an 'inertial adjustment' of the basic profiles (11), similar in principle to certain 'convective adjustment' schemes that are used to parameterize the effects of convective turbulence on large-scale variables in numerical models of atmospheric circulations. We assume that when Γ is predicted to be less than zero, or (11) satisfies (16), roll turbulence forms spontaneously over the range of r for which this is true and instantaneously reduces the zonal shear to the neutrally stable value. This process typically occurs in a region extending some distance in from the wall, and happens during the single phase of the driving cycle for which the shear is negative at $r = 0$. While this hypothesis sets the slope of the zonal velocity profile within the unstable region, it is also necessary to specify the mean velocity. Since there necessarily will be a zonal momentum flux into the wall, we anticipate a thin diffusive boundary layer between the adjusted region and $r = 1$ that carries the flux and exerts a stress on the wall. If the turbulence mixes zonal momentum efficiently, the mean velocity in the adjusted region should be about half the value of the interior flow minus that at the wall (zero). Then a second diffusive layer will appear near the boundary between the adjusted region and the interior motion. To keep the model as simple as possible we assume that this second viscous layer is similar in structure to the wall layer. This is consistent with qualitative visual observations of the experiments. During the roll-turbulence phase these show a radial slab of turbulent fluid sandwiched between the interior and the wall, and this slab seems to rotate at a rate that is less than the interior swirl, with an apparent jump in velocity between the turbulent and interior regions.

The formal adjustment procedure is carried out as follows. We first find the time at which an inertially unstable region exists. Denoting the minimum radius at which $\Gamma < 0$ as $r_c(t)$, we amend the velocity profile in the region $r_c < r < 1$ by writing

$$v(r,t) = (-cr+d)\left(1+\left(\frac{b}{d-cr_c}-1\right)e^{-\kappa(r-r_c)}-e^{\kappa(r-1)}\right). \tag{19}$$

In (19), c is the absolute value of the inertially neutral slope γ_m^{-1}, $b = v(r_c, t)$, $d = [b+c(r_c+1)]/2$, and κ^{-1} is the e-folding thickness of the thin diffusive layers on each side of the adjusted region. These narrow shear layers match velocities in the interior and bring them to zero at the wall. In order to ensure that $v(r, t)$ has continuous derivatives at $r = r_c$ we apply a smoother in the region $r_c-\epsilon \leqslant r \leqslant r_c+\epsilon, \epsilon \ll 1$. The smoother typically influences 3 to 5 points on the stretched grid in the boundary layer.

We adjust the profile using (19) until the inertially unstable region achieves its maximum extent into the interior, which occurs at time t_c (not related to r_c). At this

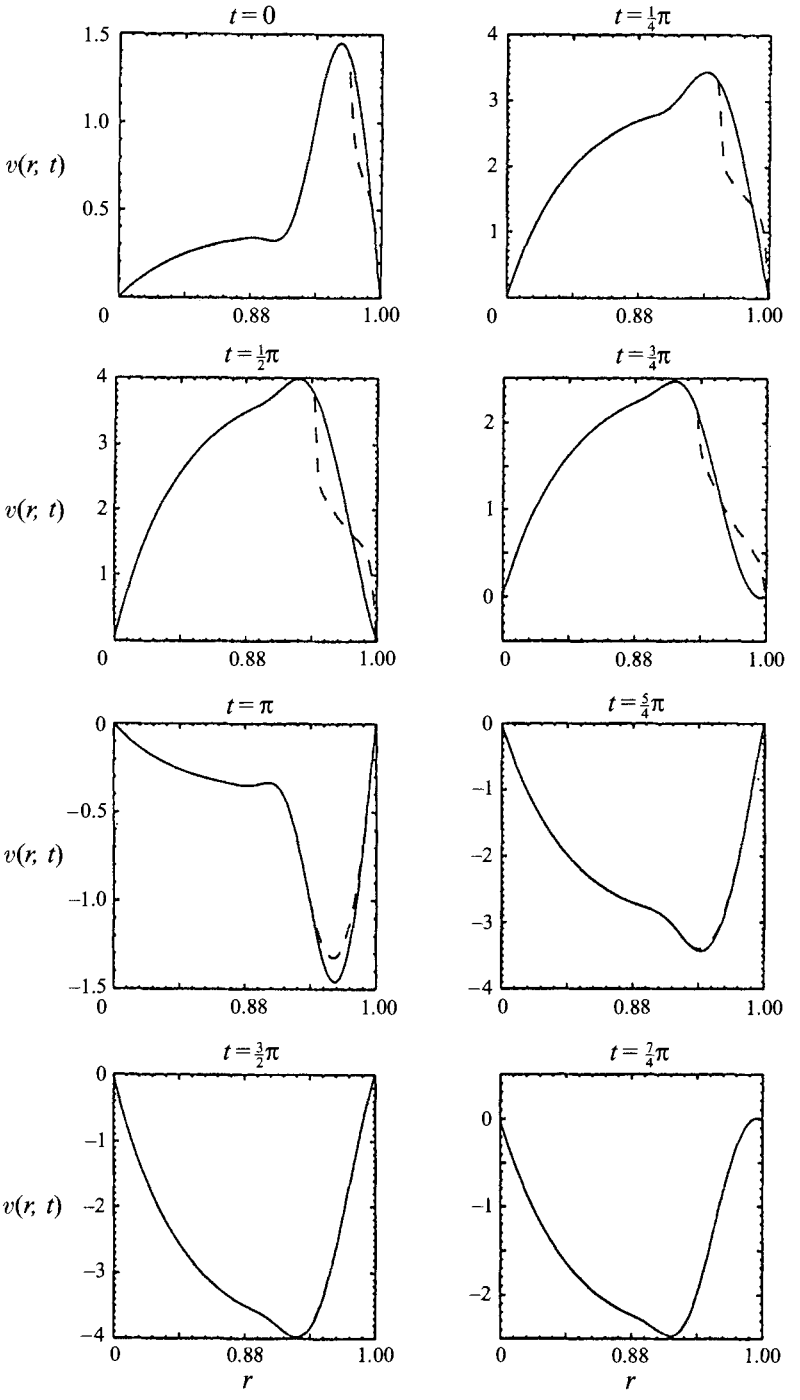

FIGURE 6. Original laminar (solid) and inertially adjusted (dashed) basic-state velocity profiles for $E = 1.6 \times 10^{-4}$, $Q = 0.1$, $\delta/\gamma_m = 8$, $\bar{\omega} = 0$ for the times shown. The minimum basic-state rotation is at $t = \frac{1}{2}\pi$, while the maximum is at $t = \frac{3}{2}\pi$. The profiles are plotted on a stretched grid to bring out detail in the boundary layer region.

time we start to relax the basic flow back to the exact laminar solution. If we denote the difference between the adjusted and unadjusted profiles at t_c as Δv_{t_c}, the total velocity for $t > t_c$ is given by

$$v(r, t) = v_{qg}(r, t) + \Delta v, \tag{20}$$

where v_{qg} is the original profile (i.e. (11)), and $\Delta v(r, t - t_c)$ is found by solving

$$\frac{\partial \Delta v}{\partial t} = \chi \nabla^2 \Delta v \tag{21}$$

with $\Delta v = \Delta v_{t_c}$ initially, and $\Delta v = 0$ at $r = 0, 1$. The relaxation constant χ is chosen so that $\Delta v \simeq 0$ by the time the cycle forcing repeats itself and inertial instability occurs again. Figure 6 shows the normal laminar and adjusted profiles for typical laboratory settings with $\kappa = 1000$ and $\chi = 0.0002$. For the supercritical situation shown, the adjustment region is widest at $t = \frac{1}{2}\pi$, since this is the time at which inertial instability first occurs. The plot shows that the flow relaxes back to the Stokes–Stewartson profile at about the time of maximum basic rotation ($t = \frac{3}{2}\pi$).

The effects of the adjustment parameters κ, ϵ and χ on the columnar-mode stability problem, based on the modified basic-state profiles such as those in figure 6, were tested empirically. The results for $\kappa = 250$, 500, 1000 and 2000 were very similar for all but the smallest value of κ. In this latter case the diffusive layers penetrate substantially into the turbulent region. Reasonable changes in the size of the smoothing width (ϵ) had no qualitative effect on the results. The parameter χ is constrained by the observation of the absence of wall turbulence during about half of the cycle. However, the instability is largely insensitive to χ because the growth occurs during the times $t < t_c$, when inertial adjustment, not relaxation, is happening. Admittedly, the inertial adjustment process is a rough approximation to the complex laboratory motions, to be tried in the face of the extremely difficult problem of simulating the entire multi-scale three-dimensional flow numerically. On the other hand, it is, as described below, rather successful in reducing the dramatic factor-of-ten disagreement between experiment and laminar-profile stability theory to essentially nil.

5. Stability results using adjusted profiles

The linearized form of (10) is again solved numerically as an initial value problem, but now using adjusted $v(r, t)$ profiles for the basic state. We fix $\Omega_0 = 2.5$ rad s^{-1}, $E = 1.6 \times 10^{-4}$, $\gamma_m = 0.025$, $Q = 0.1$, $\alpha = 4$, $\kappa = 1000$, number of gridpoints = 200, number of time steps = 2000 per cycle (typically), $\epsilon = 0.003$ (smoothing over 5 points on the stretched grid), $\chi = 2 \times 10^{-4}$, and vary k, δ and $\bar{\omega}$. Figure 7 demonstrates that the adjusted profiles are significantly more unstable than the purely laminar basic states. Note that significant amplification occurs from phase angle $t \approx \frac{1}{2}\pi$ to $t \approx \pi$ during each forcing cycle. Recall that the laboratory observations show precisely this same behaviour, with eddies forming and erupting from the boundary layer just after the deepest penetration of the small-scale sidewall turbulence. As expected, there is now only one growth phase per cycle (as opposed to two for the laminar profiles), because inertial instability only occurs when the sidewall vorticity is opposite to the basic rotation. The instability calculations predict a band of unstable waves from a lower cutoff of $k \approx 10$ to $k \approx 50$, with the latter value being the highest k tested. There is a shallow peak in amplification for waves with $k \approx 30$. Potentially significant transient instability is also found for a small range δ/γ_m just below those values required for

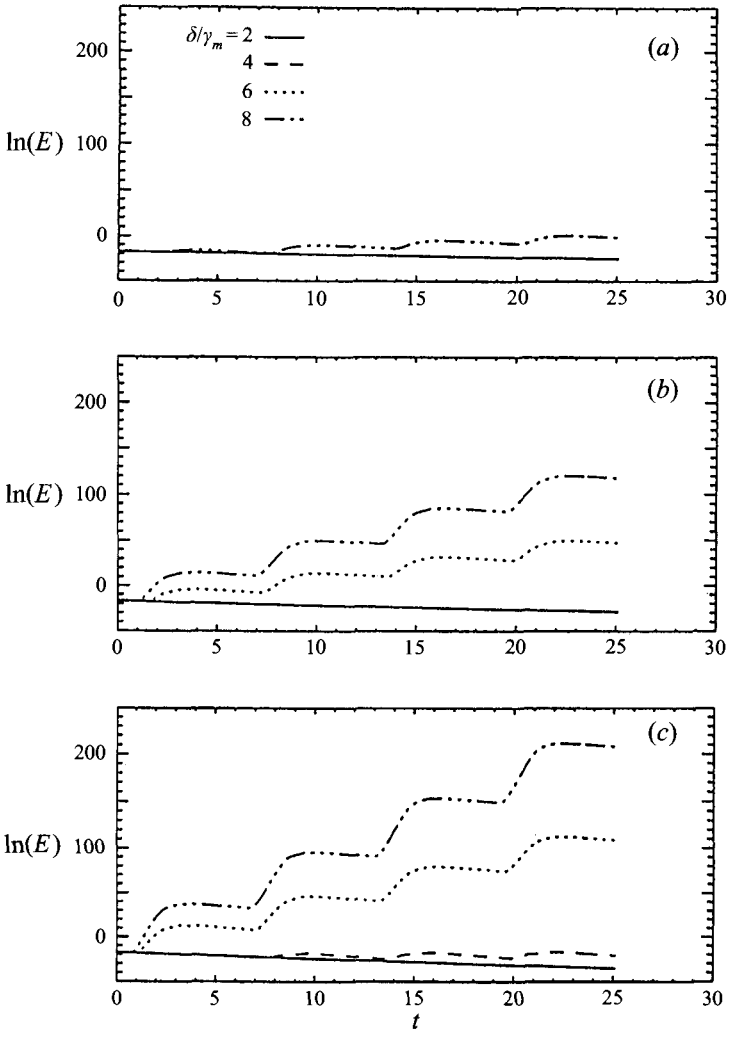

FIGURE 7. Evolution of the natural log of the kinetic energy of linear modes superimposed on the inertially adjusted basic-state profiles, with the azimuthal wavenumber shown. $E = 1.6 \times 10^{-4}$, $Q = 0.1$, $\bar{\omega} = 0$, $\gamma_m = 0.025$. (*a*) $k = 10$, (*b*) $k = 20$, (*c*) $k = 30$.

total instability (see figure 7*c*). The fact that the experiments have vortex counts corresponding to lower k, between 15 and 20, may arise by spatial subharmonic generation or by nonlinear selection of lower wavenumbers in the instability band. The columnar instability model has a basic state that has been adjusted to account for the presence of turbulence, but the lateral viscous damping of the wavy disturbances in the calculation is still accomplished by simple Newtonian friction. The direct effect of residual turbulence on the high wavenumbers in the linear mode spectrum is unknown, but it is possible that enhanced damping of such waves could occur.

Figure 8 shows adjusted profiles for a case having a mean differential rotation with $\bar{\omega}/\gamma = 4.5$. As noted above, the presence of a co-rotating differential driving increases the anticyclonic shear at the wall so that the radial width of the adjusted region is larger. Alternatively, for $\bar{\omega} > 0$ the inertial instability sets in earlier in time and remains on longer as δ/γ_m is increased. For this situation, not surprisingly, the columnar

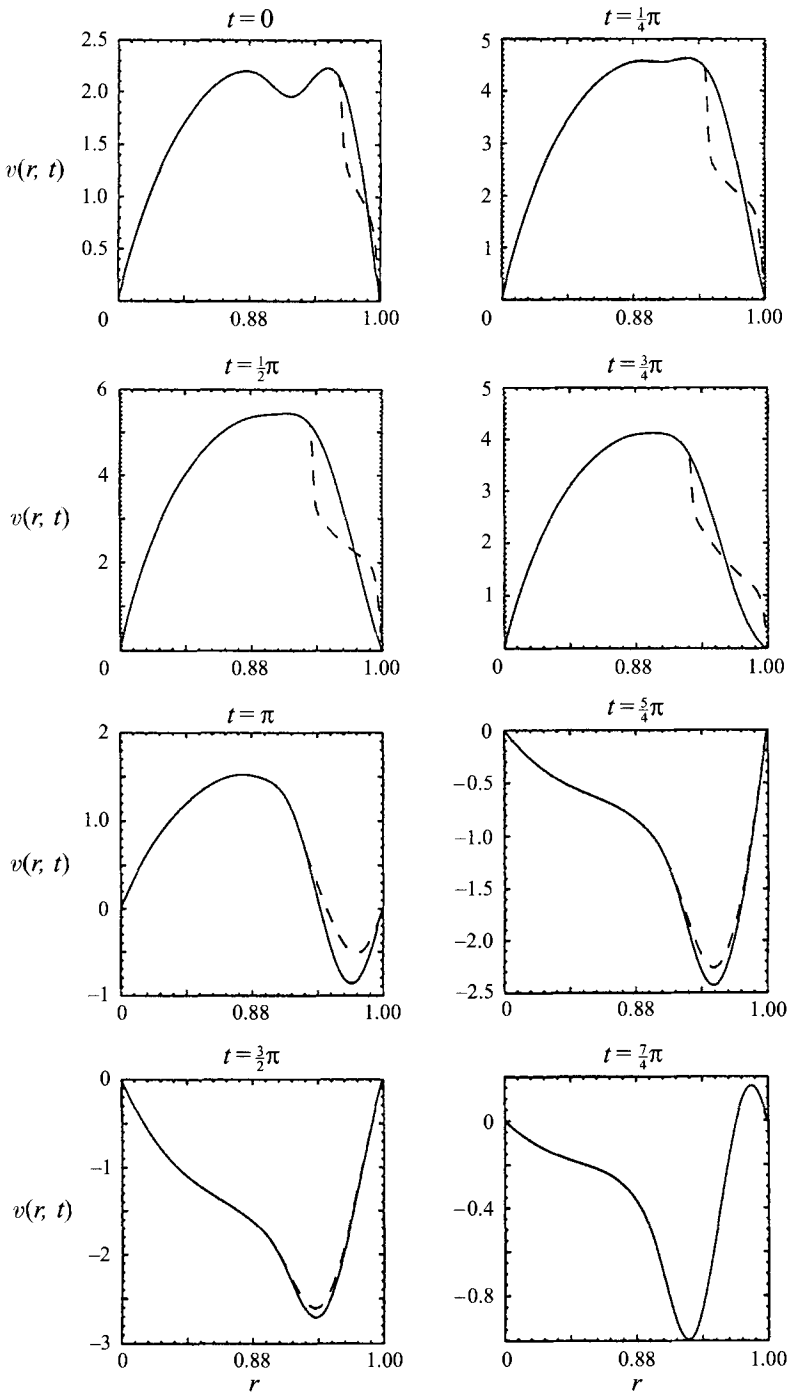

FIGURE 8. Original laminar (solid) and inertially adjusted (dashed) basic-state velocity profiles for $E = 1.6 \times 10^{-4}$, $Q = 0.1$, $\delta/\gamma_m = 8$, $\bar{\omega}/\gamma = 4.50$, for times as shown.

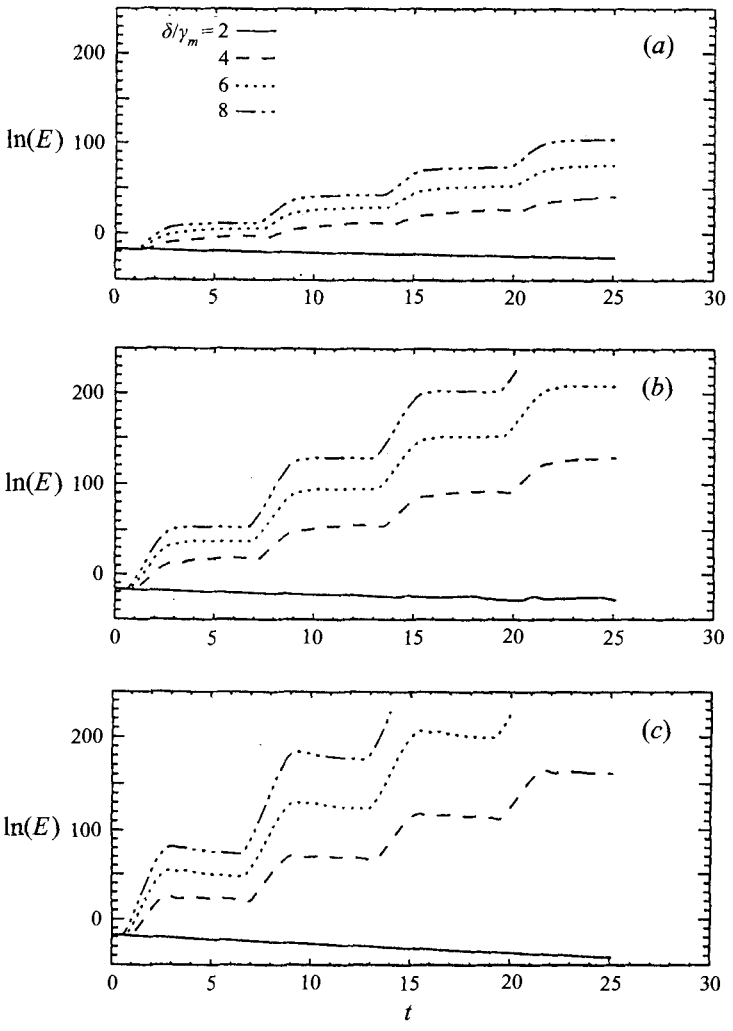

FIGURE 9. Evolution of the natural log of the kinetic energy of linear modes with the azimuthal wavenumber shown. $E = 1.6 \times 10^{-4}$, $Q = 0.1$, $\bar{\omega}/\gamma = 4.5$, $\gamma_m = 0.025$. (*a*) $k = 10$, (*b*) $k = 20$, (*c*) $k = 30$.

instabilities grow more readily. A comparison of figures 9 and 7 for $k = 20$ at the same values of δ/γ_m shows the much higher growth rates for instability with positive $\bar{\omega}$.

Combining data from a large number of computational runs for the typically observed value of $k = 20$ yields the theoretical critical curve shown in figure 10. This illustrates again that the columnar instability is stronger for positive mean differential forcing. For $\bar{\omega}/\gamma$ between -1 and 5 there is very good agreement with the experimental data in figure 3. The theoretical critical value for $\bar{\omega}/\gamma = 0$ is $\delta/\gamma_m \approx 4.6$, while for $\bar{\omega}/\gamma = 3$ onset occurs at $\delta/\gamma_m \approx 2.7$. The corresponding experimental values are 4.2 and 2.8 respectively. Although it is possible to improve or worsen the agreement by a few percent by altering the adjustment model's parameters, we have found the stability curve to be quite robust with respect to changes in κ, ϵ and χ. The important point is that the inertially adjusted instability calculation captures the main features of the experiments over a substantial range of $\bar{\omega}$. On the other hand, as shown in §3, the instability theory based on the exact laminar profile does not come close at all.

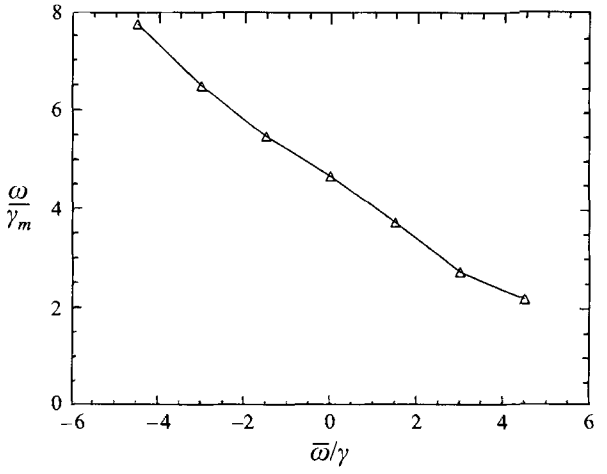

FIGURE 10. Theoretical critical curve for total instability of $k = 20$ waves based on inertially adjusted profiles. $E = 1.6 \times 10^{-4}$, $Q = 0.1$, $\gamma_m = 0.025$.

For negative mean rotation there are increasingly significant differences between theory and experiment as the counter-rotational lid forcing becomes stronger. The model critical curve becomes too high for $\bar{\omega}/\gamma \lesssim -2$. As a possible explanation, we note that the inertial adjustment is triggered when the necessary condition for inertial roll instability is satisfied. This trigger is based on linear quasi-geostrophic dynamics (i.e. (11) and (17)). However, the time-averaged Stewartson layer part of the motion driven by the mean differential rotation of the upper lid (the first terms in (11)) is accompanied by a transverse circulation associated with vertical fluxes out of the Ekman layers at the top and bottom of the sidewall layer. The effects of these ageostrophic meridional motions, other than simple stretching of mean vorticity $2\Omega_0$, are not included in the basic model (10). If $\bar{\omega} < 0$, the mean sidewall boundary flow is cyclonic, and the transverse circulation is radially outward in the layer so it will push the entire Stokes–Stewartson structure up against the sidewall.

Hart (1995) analyses this problem for a steadily forced Stewartson layer, incorporating nonlinear Ekman suction effects and stretching of total vorticity as well as ageostrophic advection. This analysis shows that the degree of sidewall boundary layer compression can be substantial if the local Rossby number across the layer, $\omega L/2\Omega_0 L_s$, where L_s is the Stewartson layer width, becomes of order one. At $\bar{\omega}/\gamma = -6$ this parameter is about 0.9 in the experiments. The net result is to increase the shear $\partial v/\partial r$ at the wall. During the phase of the forcing cycle when this is negative, the likelihood of roll turbulence will thus be enhanced, leading to more columnar instability in the experiment than in the model. The experimental stability curve should thus decrease, with respect to what happens without these higher-order Rossby number effects (i.e. figure 10) as $\bar{\omega}/\gamma$ become increasingly negative, as observed.

The above explanation should work the other way around for positive $\bar{\omega}$, because anticyclonic sidewall layers are widened by ageostrophic effects (Hart 1995). If one considers $k = 30$, or transient instead of total instability, the critical curve in figure 10 is lowered by about 10% for each change. Thus one might say that the experiment is becoming quantitatively less unstable than the model at large positive values of $\bar{\omega}/\gamma$. However, there is clearly an asymmetry in the experimental critical point data in figure 3. We observe strong destabilization at large negative $\bar{\omega}$ and only relatively weak stabilization at large positive values of $\bar{\omega}$ associated with the slight upturn of the

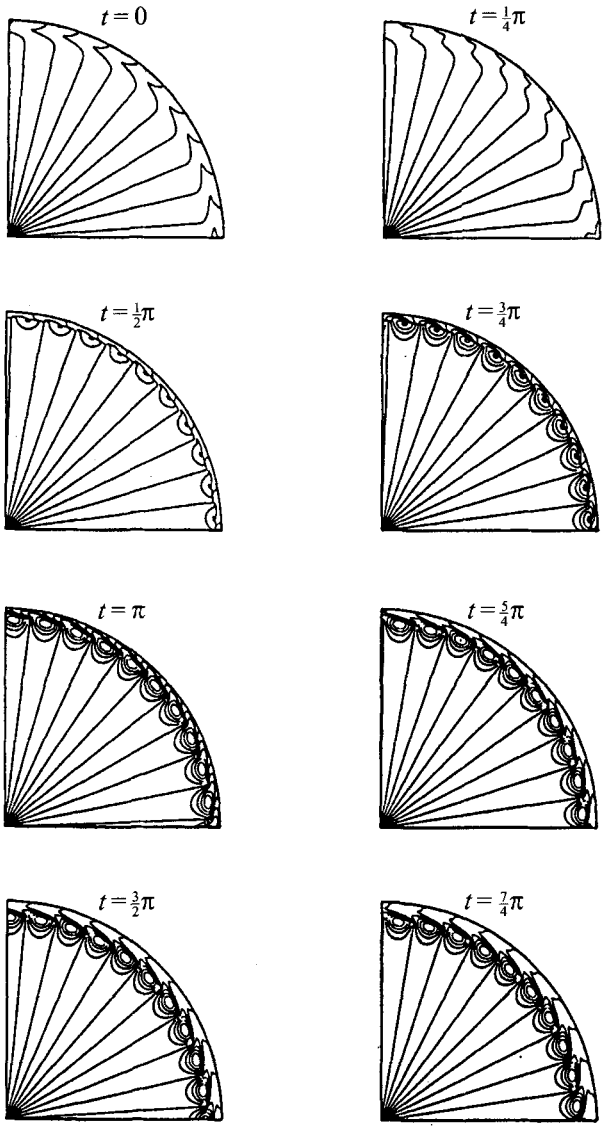

FIGURE 11. Disturbance streamfunctions computed numerically from the linear stability problem for the $k = 20$ mode with $\delta/\gamma_m = 8$, $\bar{\omega} = 0$. Contours are scaled logarithmically and are normalized by setting the maximum contour equal to 1 based at the time of maximum amplitude, which occurs at $t \approx \frac{5}{4}\pi$. The radial coordinate is not stretched.

transition curve for $\bar{\omega}/\gamma$ between 4 and 6. This might be related to Ro^2 corrections in the boundary layers (in addition to the Ro corrections speculated in the previous paragraph). We prefer the explanation that the asymmetry is due to the nature of the lid-driving setup itself. There is a near-singular vertical vorticity region in the small 1 mm gap where the differentially rotating disc meets the sidewall. When the lid is co-rotating ($\bar{\omega} > 0$) the Ekman layer flow just beneath the top lid is outwards, and the large negative vorticity in the top corner can be advected down into the sidewall boundary layer by this Ekman flux. Roll instabilities in the sidewall boundary layer under conditions of steady differential lid forcing have been observed in the laboratory to be much enhanced by this effect (Hart & Kittelman 1995). However, for counter-

rotation of the top lid the Ekman radial flow is up the sidewall and then radially inwards in the Ekman layer, and the near-singular vorticity is restricted to the gap. This gap effect may counter the expected stabilization by ageostrophic circulations for positive $\bar{\omega}$.

With δ, $\bar{\omega}$, and Ω_0 fixed, the columnar instability observed in the laboratory cuts off at both large and small γ_m, relative to that required for maximum vortex generation (≈ 0.03). As the modulation frequency decreases (small γ_m), the Stokes layer widens and eventually the trigger for inertial adjustment is not activated. It can be shown that the observed loss of columnar modes at the low-frequency limit cited at the end of §2 corresponds to a situation where the flow is nearly marginal with respect to the trigger condition (17). At the high-frequency end, although the necessary condition for inertial instability is satisfied for a sizeable fraction of the modulation cycle, the cycle is so short that roll instability and turbulence do not have time to develop and are less effective at modifying the laminar profile.

Lastly, the spatial structures from the adjusted linear problem are quite suggestive of the observed columnar eddies. Figure 11 illustrates the nature of the instability in space and time by showing the evolution of the perturbation streamfunction for a specific k over a cycle of the forcing. The waves amplify in the shear layer right next to the wall starting at about $t = \frac{1}{2}\pi$. As they grow they propagate away from the boundary. For the situation shown, there is a net amplification between $t = 0$ and $t = 2\pi$. The penetration of the waves into the interior is similar to what is observed in the experiments, although the amplification is generally large enough that the experiments are strongly influenced by columnar nonlinear effects once the eddies have escaped the near-wall turbulent region.

6. Conclusions

Laboratory observations of periodically forced flow in a rapidly rotating cylinder, which is also subject to driving by mean differential rotation of the upper lid, show columnar vortex generation by instability in the sidewall boundary layer. The vortices are invariant with distance along the axis of rotation, in concert with the Taylor–Proudman constraint. An exact axisymmetric solution of the depth-invariant quasi-geostrophic vorticity equation is obtained. This basic-state flow takes the form of periodic solid rotation of the interior coupled to the wall via a Stokes oscillatory boundary layer that is modified by vortex stretching induced by Ekman suction. Thus, this solution is called a Stokes–Stewartson layer. Linear instability calculations for non-axisymmetric perturbations show that this profile is very stable, with a critical point a factor of 10 larger than what is required for wavy vortices in the experiments.

This discrepancy is addressed by taking account of the effects of small-scale Taylor-vortex-like 'inertial instability' near the wall. We use an inertial adjustment scheme in which the fine-structure turbulence is proposed to render the mean profile neutral to inertial instability, when conditions favour such, followed (in time) by a viscous relaxation back to the exact solution during the inertially stable phase of the driving cycle. The columnar mode stability problem is then recalculated using these modified profiles. The inertially adjusted flows are found to be much more unstable, with critical parameters that are in good agreement with those found experimentally. The exceptions that occur when the periodic modulation of the basic rotation is supplemented by a large time-mean forcing at the upper lid are thought to be due to ageostrophic advections in the sidewall boundary layer that are not a part of our model.

To further explore the idea that small-scale roll instability and turbulence can alter the mean state and lead to large-scale coherent structure generation, direct measurements of the vertically averaged azimuthal flow $\bar{v}(r, t)$, or possibly computational simulation of it, are suggested. Probing the 4 mm thick sidewall Stokes layer with sufficient precision and resolution is a difficult task, but two-dimensional stretched-grid computational simulations in r and z may provide insights into the formation of profiles like those shown in figures 6 and 8. The present results illustrate the danger of using eddy viscosity concepts to generate zonal flows that are subsequently tested for instability (or may be expected to be unstable). Here, small-scale turbulence within the sidewall boundary layer acts in a very different way than viscosity in shaping the azimuthal basic flow, and renders this zonal flow highly unstable to columnar vortical disturbances.

Mr Stefan Winnerl performed several preliminary laboratory experiments and Mr Scott Kittelman assisted with the apparatus. We gratefully acknowledge support of this research by the National Science Foundation through grant OCE-92-02995 to the University of Colorado.

REFERENCES

BEARDSLEY, R. C. 1969 A laboratory model of the wind driven ocean circulations. *J. Fluid Mech.* **38**, 255–271.

BEARDSLEY, R. C. 1975 A 'sliced-cylinder' laboratory model of the wind-driven ocean circulation. Part 2. Oscillatory forcing and Rossby-wave resonance. *J. Fluid Mech.* **69**, 41–64.

DAVIS, S. H. 1976 The stability of time-periodic flows. *Ann. Rev. Fluid Mech.* **8**, 57–74.

HART, J. E. 1971 Instability and secondary motion in a rotating channel flow. *J. Fluid Mech.* **45**, 341–348.

HART, J. E. 1990 On oscillatory flow over topography in a rotating fluid. *J. Fluid Mech.* **214**, 537–454.

HART, J. E. 1994 Sidewall instability and eddy generation in a rotating fluid subject to periodic forcing. *Appl. Mech. Rev.* **47**, S118–S122.

HART, J. E. 1995 Nonlinear Ekman suction and ageostrophic effects in rapidly rotating flows. *Geophys. Astrophys. Fluid Dyn.* **79**, 201–222.

HART, J. E. & KITTELMAN, S. 1995 Instabilities of the sidewall boundary layer in a differentially driven rotating cylinder. *Phys. Fluids* (submitted).

JOHNSTON, J. P., HALLEEN, R. M. & LEZIUS, D. K. 1972 Effects of spanwise rotation on the structure of two-dimensional fully developed turbulent channel flow. *J. Fluid Mech.* **56**, 533–557.

KERCZEK, C. VON & DAVIS, S. H. 1974 Linear stability theory of oscillatory Stokes layers. *J. Fluid Mech.* **62**, 753–773.

KRISHNAMURTI, R. 1981 Laboratory modelling of the oceanic response to monsoonal winds. In *Monsoon Dynamics* (ed. J. Lighthill & R. P. Pearce), pp. 557–576. Cambridge University Press.

PRATTE, J. M. & HART, J. E. 1991 Experiments on periodically forced flow over topography in a rotating fluid. *J. Fluid Mech.* **77**, 153–175.

STEWARTSON, K. 1957 On almost rigid rotations. *J. Fluid Mech.* **3**, 17–26.

STOKES, G. G. 1851 On the effect of internal friction of fluids on the motion of pendulums. *Trans. Camb. Phil. Soc.* **9**, 8–106.

TAFTI, D. K. & VANKA, S. P. 1991 A numerical study of the effects of span-wise rotation on turbulent channel flow. *Phys. Fluids* A **3**, 642–656.